Kinetics of B2- and $D0_3$-type ordering and formation of domain structures in Fe–Al alloys

2008 J. Phys.: Condens. Matter 20 275225

(http://iopscience.iop.org/0953-8984/20/27/275225)

J. Phys.: Condens. Matter **20** (2008) 275225 (9pp) doi:10.1088/0953-8984/20/27/275225

Kinetics of B2- and $D0_3$-type ordering and formation of domain structures in Fe–Al alloys

R Oguma[1], S Matsumura[2] and T Eguchi[1]

[1] Department of Applied Physics, Fukuoka University, Nanakuma 8-19-1, Jonanku, Fukuoka 814-0180, Japan
[2] Department of Applied Quantum Physics and Nuclear Engineering, Kyushu University, Fukuoka 819-0395, Japan

E-mail: oguma@fukuoka-u.ac.jp

Received 19 June 2007, in final form 12 May 2008
Published 6 June 2008
Online at stacks.iop.org/JPhysCM/20/275225

Abstract

Time-dependent Ginzburg–Landau (TDGL) formulation has been developed for the ordering processes of B2 and $D0_3$ types in binary alloy systems. In the formulation, three order parameters are defined in order to describe the state of order. Equivalent variants of B2 and $D0_3$ structures are distinguished using these order parameters. The mean-field free energy is defined in the form of a Landau-type expansion using the order parameters and a composition parameter. Interface energies due to local variations in the degrees of order and concentration are given with a gradient square approximation. Kinetic equations are derived from the Ginzburg–Landau-type potential in order to describe the time-evolutions of the order parameters and the concentration. Numerical simulations of the kinetic equations have been performed for B2- and $D0_3$-type ordering as well as concurrent ordering and phase separation to disordered A2 + $D0_3$. The simulated results provide a good reproduction of the formation processes of B2 and $D0_3$ ordered domains in an Fe_3Al alloy.

1. Introduction

The substitutional solid solutions of an iron-rich Fe–Al binary alloy system form ordered structures B2 and $D0_3$ that are based on the fundamental bcc crystal lattice. Figure 1 shows a part of the equilibrium phase diagram of Fe–Al with around 25 at.% Al [1]. The composition-temperature ranges in which the ordering of B2 and $D0_3$ occurs can be confirmed from figure 1. Here, A2 is the disordered phase of a bcc solid solution. The regions of A2, B2, and $D0_3$ phases are divided with single lines in the Al-rich side of figure 1. This indicates that the phase transitions between A2 and B2 as well as between B2 and $D0_3$ occur on the lines in a manner classified as the second order. The transition line A2–B2 ends in a tricritical point at approximately 23 at.% Al and 890 K. A miscibility gap extends between the A2 and B2 phases below this point. As the B2–$D0_3$ transition line impinges on the miscibility gap, a two-phase mixture of A2 and $D0_3$ appears in the lower temperature portion of the miscibility gap. The crystal structures of A2, B2, and $D0_3$ are illustrated in figure 2. In the A2 phase, atoms of the elements of A and B randomly occupy the bcc lattice sites. The B2 structure is formed by the ordering reaction of A and B atoms between the first nearest neighbors. It comprises two simple-cubic-type sublattices with different compositions. In the B2 phase, two types of variants exist depending on which of the two sublattices are preferably occupied by the A and B atoms. Antiphase boundaries (APBs) with displacement $a/4\langle 111\rangle$ are formed where the two variants come into contact. Here, a is the lattice constant of the unit cells shown in figure 2. If additional ordering occurs between the second nearest-neighbor atoms, the ordered state changes from B2 to $D0_3$. The stoichiometry of $D0_3$ is A_3B in contrast to AB for B2. In the perfect $D0_3$-type order at A_3B, B atoms form an fcc sublattice, as denoted by the unfilled circles in figure 2(c). Therefore, the four types of variants are defined in $D0_3$ depending on the position of the fcc sublattice enriched with B atoms. The $D0_3$ ordered phase is partitioned into antiphase domains by APBs with a displacement of $a/4\langle 111\rangle$ or $a/2\langle 100\rangle$. In the last

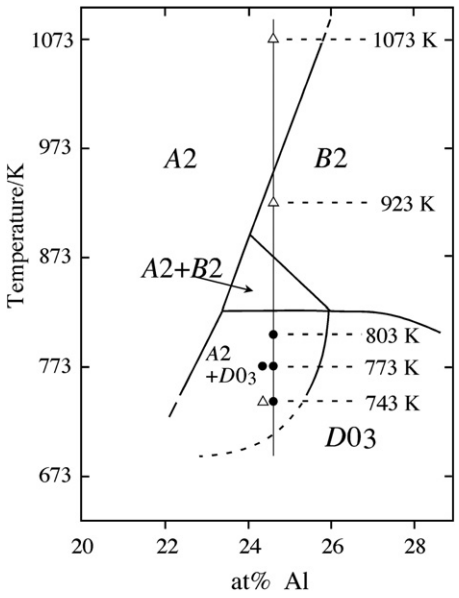

Figure 1. The relevant portion of the equilibrium phase diagram of Fe–Al [1]. Filled circles and open triangles denote heat-treatment temperatures of Fe–24.6 at.% Al alloy in the experiment.

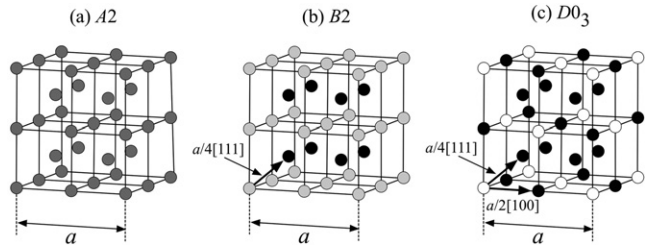

Figure 2. Crystal structures of A2 (a), B2 (b), and $D0_3$ (c) and displacement vectors of APBs.

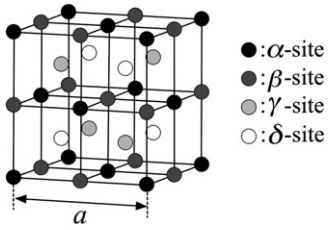

Figure 3. Definition of the four fcc sublattices α, β, γ, and δ.

few decades, the formation of antiphase domain structures and their time-evolution have been attracting considerable interest from both the fundamental and applied or practical viewpoints of ordering alloys. Extensive observations by transmission electron microscopy (TEM) have revealed the occurrence of microstructural changes due to ordering as well as ordering with phase separation in Fe–Al alloys [2–11]. The specific features of microstructural evolution are inherently related to the crystal symmetry changes due to the relevant ordering reaction. Therefore, the kinetic modeling and analysis of the processes should consider the symmetrical aspects of ordered structures. A microscopic formulation based on a discrete lattice can easily include the crystal symmetrical changes due to ordering [12–24]. However, it is sometimes difficult to analyze domain growth behavior over a wide range of length scale because it is at a microscopic scale. In contrast, a mesoscopic time-dependent Ginzburg–Landau (TDGL) model on a continuous medium [25–28] is useful for studying the latter [5, 7, 9, 28–33]. Eguchi *et al* [29], Shiiyama *et al* [31, 32], and Matsumura *et al* [33] have successfully simulated processes involved in B2 ordering and the evolution of the two variant phases with TDGL equations for concentration variation and degree of order. However, no mesoscopic model has been presented for the case with more than two variants in $D0_3$-type ordering.

In this study, we define a free energy function by using a Landau expansion for the B2 and $D0_3$ ordered phases, considering their symmetry relationships on a continuous medium. Therefore four types of variants of $D0_3$ ordered phase are taken into account in our formulation. The kinetic equations for the ordering processes are derived in TDGL forms with the obtained free energy function and are then applied to simulate the time-evolution of B2- and/or $D0_3$-type ordering: B2 $\rightarrow$ $D0_3$, A2 $\rightarrow$ $D0_3$, B2 $\rightarrow$ A2 + $D0_3$, and A2 $\rightarrow$ A2 + $D0_3$. The two-dimensional microscopic models given by Vaks *et al* well reproduced formations of domain structures in various types of ordering of B2 and/or $D0_3$ [23, 24]. Our present model explains more clearly the domain structures in an Fe–Al alloy by comparing microstructural changes obtained from three-dimensional simulations with the experimental results of TEM observations. Allen *et al* gave mesoscopic models for ordering processes, and discussed details of interface motion and domain growth with extensive TEM observations [3–10]. We evaluate interfacial tensions of boundaries simply on the basis of studies of Cahn *et al* [34] and Allen *et al* [5], and consider boundary structures from the results of the simulations.

2. Atomic occupation probabilities and representation of variants

We now consider a binary alloy system $A_{3-\varepsilon}B_{1+\varepsilon}$, which undergoes B2 and $D0_3$ ordering reactions depending on the temperature and composition. Here, ε denotes the composition deviation from the stoichiometry A_3B. To treat the structures of A2, B2, and $D0_3$ in the same framework, the fundamental bcc lattice is divided into four fcc sublattices labeled as α, β, γ, and δ which are illustrated in figure 3. The site occupation probabilities of the constituent elements are given as a function of three order parameters ξ, η, and ζ and the composition deviation ε, as listed in table 1. If P_i is defined as the probability of finding B atoms on sublattice i ($i = \alpha, \beta, \gamma$, or δ), the disordered A2 state is given by $P_\alpha = P_\beta = P_\gamma = P_\delta = (1+\varepsilon)/4$ and $\xi = \eta = \zeta = 0$, while B2 is characterized by $P_\alpha = P_\beta \neq P_\gamma = P_\delta$, or $\eta \neq 0$ and $\xi = \zeta = 0$. The two types of variants of B2 are distinguished by the sign of η. As additional ordering on B-rich sublattices results from B2 in $D0_3$, the latter state of order is described by $\xi \neq 0$

Table 1. Atomic occupation probabilities close to stoichiometric composition $A_{3-\varepsilon}B_{1+\varepsilon}$ for the lattice sites defined in figure 3.

Site	A-atom	B-atom
α	$\frac{1}{4}(3-\varepsilon+\eta+2\xi)$	$\frac{1}{4}(1+\varepsilon-\eta-2\xi)$
β	$\frac{1}{4}(3-\varepsilon+\eta-2\xi)$	$\frac{1}{4}(1+\varepsilon-\eta+2\xi)$
γ	$\frac{1}{4}(3-\varepsilon-\eta+2\zeta)$	$\frac{1}{4}(1+\varepsilon+\eta-2\zeta)$
δ	$\frac{1}{4}(3-\varepsilon-\eta-2\zeta)$	$\frac{1}{4}(1+\varepsilon+\eta+2\zeta)$

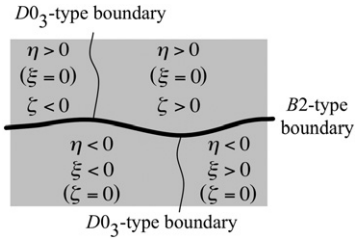

Figure 4. Order parameters satisfying the selection rule within four types of $D0_3$ domains. Thick and thin curves indicate B2- and $D0_3$-type boundaries, respectively.

and $\zeta = 0$ for $\eta < 0$ or $\xi = 0$ and $\zeta \neq 0$ for $\eta > 0$. It follows that ordered domains with negative or positive η are further partitioned into subdomains distinguished by the sign of ξ or ζ in the $D0_3$ phase. The APBs in the $D0_3$ order phase are classified into two types depending on the order parameters involved: APBs due to a change in the sign of η along with the replacement of ξ and ζ and APBs at which the sign of ξ or ζ changes, as illustrated in figure 4. The former and latter APBs are hereafter called B2 and $D0_3$ types, respectively.

The crystal structure factors $F(hkl)$ for diffraction experiments are given as a function of the order parameters as follows: when h, k, and l are all even or all odd integers,

$$F(hkl) = \begin{cases} 4\{(3-\varepsilon)f_A + (1+\varepsilon)f_B\}, & \text{if } h+k+l = 4n \\ 4(f_A - f_B)(\xi \pm i\zeta), & \text{if } h+k+l = 4n \pm 1 \\ 4(f_A - f_B)\eta, & \text{if } h+k+l = 4n+2 \end{cases} \tag{1}$$

otherwise $F(hkl) = 0$. Here, f_j is the atomic scattering factor of j-atoms (j = A or B) and n is an integer. According to the selection rule for ξ and ζ depending on the sign of η mentioned above, the second types of reflections in equation (1) practically include either ξ or ζ as the variable in the structure factors. Therefore, the three order parameters ξ, η, and ζ are measurable by diffraction experiments and uniquely define an ordered state.

3. Free energy formulation for B2 and $D0_3$ order and kinetic equations for ordering processes

The free energy of a system which undergoes B2 and $D0_3$ ordering is derived in the form of a Landau expansion with the order parameters ξ, η, ζ, and ε. The simplest form of the

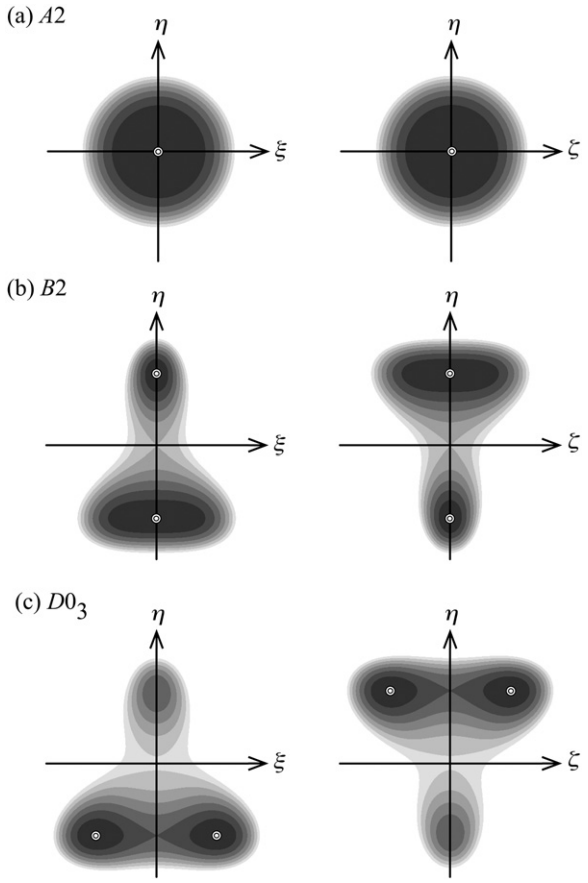

Figure 5. Contour maps of the free energy function f when states A2 (a), B2 (b), and $D0_3$ (c) are stabilized. Left and right figures are cross sections of f in ξ–η and ζ–η planes, respectively. The gray level darkens with a decrease in the value of f. Double circles indicate the minimum points at $(\xi, \eta, \zeta) = (0, 0, 0)$ for A2 state (a), $(0, \pm Y, 0)$ for B2 (b), and $(0, Y, \pm X)$ and $(\pm X, -Y, 0)$ for $D0_3$ (c).

free energy f is given as

$$\begin{aligned} f(\xi,\eta,\zeta,\varepsilon,T) = A_0(T)\{&a(T) + \tfrac{1}{2}b(T)(\varepsilon-\varepsilon_0(T))^2 \\ &- \tfrac{1}{2}(X(\varepsilon,T)^2 - Y(\varepsilon,T)^2)(\xi^2+\zeta^2) \\ &- \tfrac{1}{2}Y(\varepsilon,T)^2\eta^2 + Y(\varepsilon,T)(\xi^2-\zeta^2)\eta \\ &+ \tfrac{1}{4}(\xi^2+\eta^2+\zeta^2)^2\}, \end{aligned} \tag{2}$$

where A_0, a, b, and ε_0 are positive coefficients depending on temperature T. The parameters $X(\varepsilon, T)$ and $Y(\varepsilon, T)$ determine the stable phase state in such a manner that $D0_3$ appears when $X \neq 0$ and $Y \neq 0$, while B2 becomes stable when $X = 0$ but $Y \neq 0$. No ordering occurs if both X and Y vanish. The phase stability thus mentioned is confirmed in figure 5, where contour maps of the function f are given in the three-dimensional Euclidean space of the order parameters (ξ, η, ζ). The function f takes a minimum value at the origin $(\xi, \eta, \zeta) = (0, 0, 0)$ for $X = Y = 0$, as shown in figure 5(a), stabilizing the disordered state A2. If $X = 0$ but $Y \neq 0$, two minima appear symmetrically at $\eta \pm Y(\varepsilon, T)$ on the axis $\xi = \zeta = 0$ in figure 5(b), leading to two variants of the B2 phase. When $X \neq 0$ and $Y \neq 0$, two minima are located at points where $\zeta = \pm X(\varepsilon, T)$ and $\eta = Y(\varepsilon, T)$ in the plane of $\xi = 0$, while another two minima appear at $(\xi, \eta) = (X, -Y)$

and $(\xi, \eta) = (-X, -Y)$ in the plane of $\zeta = 0$ (see figure 5(c)). These four minima correspond to four equivalent variants of the $D0_3$ phase. Therefore, equation (2) satisfies the selection rule for the parameters ξ and ζ depending on the sign of η for $D0_3$, and qualitatively expresses the free energy of the relevant phase states A2, B2, and $D0_3$. It should be noted that the parameters X and Y give the equilibrium values of the order parameters ξ, η, and ζ. If the functions X and Y are described in such simple forms as

$$X(\varepsilon, T) = X_0(T)\sqrt{1 - \left(\frac{\varepsilon}{c_X(T)}\right)^2}, \tag{3}$$

$$Y(\varepsilon, T) = Y_0(T)\sqrt{1 - \left(\frac{\varepsilon - \varepsilon_{B2}}{c_Y(T)}\right)^2}, \tag{4}$$

the ordering reactions of the $D0_3$ and B2 types occur at a given temperature T in the composition ranges $-c_X(T) < \varepsilon < c_X(T)$ and $\varepsilon_{B2} - c_Y(T) < \varepsilon < \varepsilon_{B2} + c_Y(T)$, respectively. Here, $X_0(T)$ and $Y_0(T)$ give the equilibrium degrees of order at the stoichiometric compositions for $D0_3(\varepsilon = 0)$ and $B2(\varepsilon = \varepsilon_{B2})$, respectively, A model for the equilibrium phase diagram can be easily constructed if functions $X_0(T)$, $Y_0(T)$, $c_X(T)$, and $c_Y(T)$ are known. We set

$$\begin{aligned} X_0(T) &= \sqrt{1 - \frac{T}{823}}, \\ c_X(T) &= \frac{1}{0.9}\left(1 - \frac{T}{823}\right)^{0.47}, \\ Y_0(T) &= \sqrt{1 - \frac{T}{890}} \qquad \text{and} \\ c_Y(T) &= \frac{1}{0.43}\left(1 - \frac{T}{890}\right)^{0.4} \end{aligned} \tag{5}$$

for Fe–Al alloy systems, and obtain the model phase diagram shown in figure 6, which is comparable to figure 1.

The thermodynamic potential of a system with spatial variations in the order parameters as well as in composition is assumed in a Ginzburg–Landau form with the square gradient approximation for interface energy densities [34]:

$$\Phi = \int \{f(\xi, \eta, \zeta, \varepsilon, T) + g(\vec{\nabla}\xi, \vec{\nabla}\eta, \vec{\nabla}\zeta, \vec{\nabla}\varepsilon, T)\}\,\mathrm{d}\mathbf{r}, \tag{6}$$

$$\begin{aligned} g(\vec{\nabla}\xi, \vec{\nabla}\eta, \vec{\nabla}\zeta, \vec{\nabla}\varepsilon, T) &= \tfrac{1}{2}\nu(T)(\vec{\nabla}\xi)^2 \\ &+ \tfrac{1}{2}\mu(T)(\vec{\nabla}\eta)^2 + \tfrac{1}{2}\nu(T)(\vec{\nabla}\zeta)^2 + \tfrac{1}{2}\omega(T)(\vec{\nabla}\varepsilon)^2. \end{aligned} \tag{7}$$

Here, the gradient energy coefficients $\nu(T)$, $\mu(T)$, and $\omega(T)$ take positive values depending on the temperature. The coefficient $\nu(T)$ for $(\vec{\nabla}\xi)^2$ is equal to that for $(\vec{\nabla}\zeta)^2$ in equation (7) since ξ and ζ are defined equivalently in table 1. The temporal changes of the local state of order and local composition when the system deviates from thermal equilibrium are considered to obey the following well-known equations [26, 27],

$$\frac{\partial\xi}{\partial t} = -L_1(T)\frac{\delta\Phi}{\delta\xi}, \qquad \frac{\partial\eta}{\partial t} = -L_2(T)\frac{\delta\Phi}{\delta\eta},$$
$$\frac{\partial\zeta}{\partial t} = -L_1(T)\frac{\delta\Phi}{\delta\zeta}, \qquad \text{and} \qquad \frac{\partial\varepsilon}{\partial t} = M(T)\nabla^2\frac{\delta\Phi}{\delta\varepsilon}. \tag{8}$$

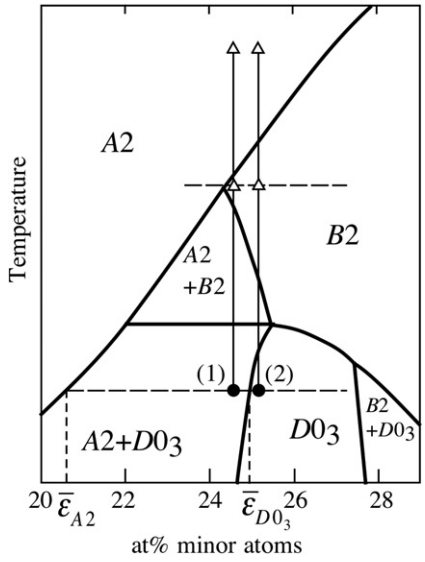

Figure 6. The model phase diagram of Fe–Al type. Two systems of Fe–Al type with $\varepsilon = -0.025$ (1), 0 (2) were considered in the simulations. Filled circles and open triangles indicate annealing temperatures in the simulations. The composition ε in the miscibility gap for the system (1) takes $\bar{\varepsilon}_{A2}$ and $\bar{\varepsilon}_{D0_3}$ within the phases A2 and $D0_3$, respectively.

Here, $L_1(T)$, $L_2(T)$, and $M(T)$ are reaction constants, and the equations for ξ and ζ take the same constant L_1. Substituting equations (6) and (7) into (8), one can derive the explicit forms of the kinetic equations as follows,

$$\begin{aligned} \frac{\partial\xi}{\partial t} &= L_1A_0\{(X^2 - Y^2)\xi - 2Y\xi\eta \\ &- \xi(\xi^2 + \eta^2 + \zeta^2)\} + L_1\nu\nabla^2\xi, \end{aligned} \tag{9}$$

$$\begin{aligned} \frac{\partial\eta}{\partial t} &= L_2A_0\{Y^2\eta - Y(\xi^2 - \zeta^2) \\ &- \eta(\xi^2 + \eta^2 + \zeta^2)\} + L_2\mu\nabla^2\eta, \end{aligned} \tag{10}$$

$$\begin{aligned} \frac{\partial\zeta}{\partial t} &= L_1A_0\{(X^2 - Y^2)\zeta + 2Y\zeta\eta \\ &- \zeta(\xi^2 + \eta^2 + \zeta^2)\} + L_1\nu\nabla^2\zeta, \end{aligned} \tag{11}$$

and

$$\begin{aligned} \frac{\partial\varepsilon}{\partial t} &= MA_0\nabla^2\left[b\varepsilon + (\xi^2 + \zeta^2)X\frac{\partial X}{\partial\varepsilon}\right. \\ &\left. + \{(\xi^2 - \zeta^2)\eta - (\xi^2 + \eta^2 + \zeta^2)Y\}\frac{\partial Y}{\partial\varepsilon}\right] - M\omega\nabla^4\varepsilon. \end{aligned} \tag{12}$$

The coupled kinetic equations of the TDGL types thus derived are expected to describe the time-evolution of B2 and/or $D0_3$ ordering processes with composition variation.

4. Simulation and experiment

The simulations of the ordering processes were performed on a three-dimensional square grid of $120 \times 120 \times 120$ mesh with periodic boundary conditions. Here, the lattice constant of the grid is regarded as a unit length. The TDGL equations (9)–(12) were transformed into difference types and the temporal changes of the order parameters at each cell in the grid were

obtained by numerically solving the difference-type equations. Here, the Laplacian of a parameter u ($=\xi, \eta, \zeta$, or ε) at (x, y, z) was evaluated by

$$\nabla^2 u(x, y, z) = \sum_{\langle \delta x_1, \delta y_1, \delta z_1 \rangle} \{u(x + \delta x_1, y + \delta y_1, z + \delta z_1) - u(x, y, z)\}. \quad (13)$$

The sum in the right-hand side runs over the first nearest-neighbor cells. The gradient energy coefficients ν, μ and ω were set to be $\nu{:}\mu{:}\omega = 0.88{:}0.44{:}1$ in the present simulations. The assumed temperatures and alloy compositions are plotted in figure 6. The simulations began from one of the homogeneous states B2 or A2. The initial values of the local composition $\varepsilon_0(x, y, z)$ were given with the overall composition ε and three individual sets of small random numbers $\{R^\varepsilon(x, y, z)\}$, $\{Q^\varepsilon(x, y, z)\}$, and $\{S^\varepsilon(x, y, z)\}$ as

$$\varepsilon_0(x, y, z) = \varepsilon + \{R^\varepsilon(x, y, z) - R^\varepsilon(x - 1, y, z) + Q^\varepsilon(x, y, z) - Q^\varepsilon(x, y - 1, z) + S^\varepsilon(x, y, z) - S^\varepsilon(x, y, z - 1)\}, \quad (14)$$

since the following conserved condition is guaranteed:

$$\sum_{x,y,z} \{R^\varepsilon(x, y, z) - R^\varepsilon(x - 1, y, z) + Q^\varepsilon(x, y, z) - Q^\varepsilon(x, y - 1, z) + S^\varepsilon(x, y, z) - S^\varepsilon(x, y, z - 1)\} = 0. \quad (15)$$

For an initial B2 state with mean degree of order $\bar{\eta}_0$, the order parameters were prepared with another three sets of random numbers around zero $\{R^\xi(x, y, z)\}$, $\{R^\eta(x, y, z)\}$, and $\{R^\zeta(x, y, z)\}$ as

$$\xi_0(x, y, z) = R^\xi(x, y, z),$$
$$\eta_0(x, y, z) = \bar{\eta}_0 + R^\eta(x, y, z), \quad (16)$$
$$\zeta_0(x, y, z) = R^\zeta(x, y, z).$$

On the other hand, when the simulation began from the A2 state, the initial values of the order parameters were set to be

$$\xi_0(x, y) = R^\xi(x, y, z) R^\eta(x, y, z),$$
$$\eta_0(x, y, z) = R^\eta(x, y, z), \quad (17)$$
$$\zeta_0(x, y, z) = R^\zeta(x, y, z) R^\eta(x, y, z),$$

to avoid non-physical situations such as $\xi(x, y, z)$ and/or $\zeta(x, y, z) \neq 0$ when $\eta(x, y, z) = 0$. The simulation results were plotted in two- or three-dimensional views. In the former, the values of the composition and the functions of the order parameters were integrated in ten layers of grids along the z direction.

In the experiment, ingots of an Fe–24.6 at.% Al alloy were prepared by the vacuum induction melting of the pure materials. The disk specimens of 3 mm diameter were homogenized for 21.6 ks at 1073 K where the A2 phase is stable. Some of the specimens were annealed at 923 K for 10 ks so that they would be ordered in a B2 state. The homogenized specimens in the A2 or B2 states were aged for a given duration at 743, 773, or 803 K. The temperatures at which the specimens were heat-treated are indicated in figure 1. Electron microscope observation was carried out using a JEM-200CX TEM at an accelerating voltage of 200 kV. The microstructures of the specimens were observed in dark field images with a 111 or 222 superlattice reflection, where the former is of the $D0_3$ type and the latter of the B2 type, as described in section 2.

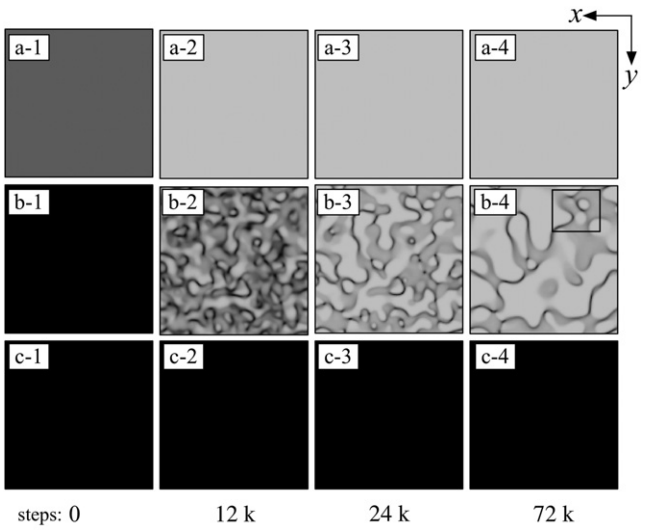

Figure 7. Example of simulated ordering processes from B2 to $D0_3$ at $\varepsilon = 0$. Top (a), middle (b), and bottom rows (c) include two-dimensional maps of positive η, ζ^2, and ξ^2, respectively. The gray level varies from dark to bright with an increase in their values. Maps (b-2)–(b-4) correspond to 111 dark field images since $\xi^2 \sim 0$ after 12 k steps. Three-dimensional maps for the region surrounded by a rectangle in (b-4) are presented in figure 8.

5. Results

5.1. $B2 \rightarrow D0_3$ transition

Figure 7 shows a simulated ordering process from B2 to $D0_3$ at the stoichiometric composition of $\varepsilon = 0$. In the initial state, the mean values of η, ξ, and ζ are $\eta = \bar{\eta}_0$, $\xi = 0$, and $\zeta = 0$, respectively, as shown in (a-1), (b-1), and (c-1). The map of η turns light gray uniformly in (a-2) after 12 k steps, indicating that the positive value of η entirely increases and becomes uniform. The spatial variation in ζ is recognized in (b-2); however, the map of ξ is still completely dark over the entire area in (c-2). The $D0_3$-type ordering develops in this stage according to the selection rule for the order parameters ξ and ζ depending on the sign of η (see figure 4). Subsequently, the $D0_3$ domains grow with time as shown in the maps of ζ^2, while no distinct change occurs in the maps of η and ξ^2. The region surrounded by a rectangle in (b-4) has been plotted in a three-dimensional data representation in figure 8. The values of ζ^2 were mapped as 'iso-order' surfaces, which correspond to $D0_3$-type APBs. Curved and intricate APBs can be recognized. The resultant morphology of the $D0_3$ domains in (b-4) is quite similar to that observed in a TEM image of the Fe–24.6 at.% Al alloy shown in figure 9.

5.2. $A2 \rightarrow D0_3$ transition

Figure 10 shows a simulated process of $D0_3$ ordering from a disordered A2 phase. A domain structure has been formed in

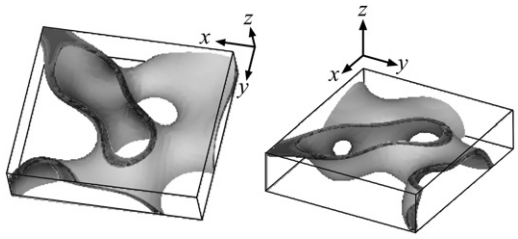

Figure 8. Three-dimensional maps of ζ^2 as iso-order surfaces for the region surrounded by a rectangle in figure 7(b-4). The surfaces are plotted in ten layers of grids along the z direction and correspond to $D0_3$-type APBs.

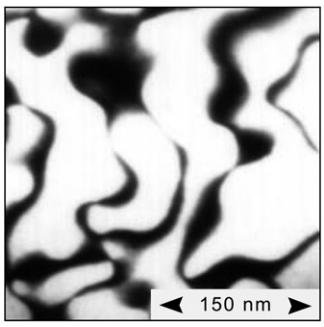

Figure 9. 111 dark field image of Fe–24.6 at.% Al alloy annealed at 743 K for 10 ks.

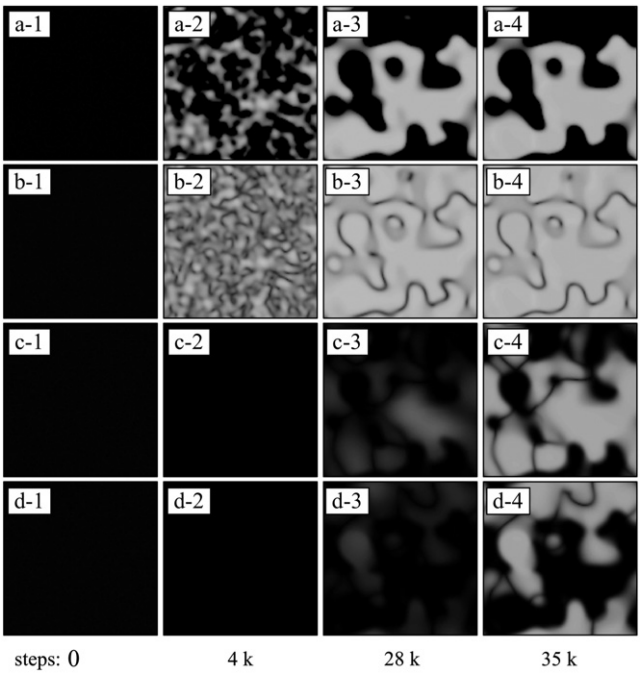

Figure 10. Time-evolution of the ordering process from A2 to $D0_3$ at $\varepsilon = 0$. Two-dimensional maps of η, η^2, ζ^2, and ξ^2 are placed from top to bottom. The gray level varies from dark to bright with an increase in their values. The selection rule of the order parameters can be confirmed by comparing these maps (see figure 4).

the map of η at 4 k steps in (a-2); however, the maps of ξ and ζ are still completely dark. It is indicated that B2-type ordering first occurs in the early stage of ordering. The B2 domains grow with time between 4 and 28 k steps as shown in (a-2) and (a-3). Subsequently, $D0_3$ ordered regions with non-zero ξ are formed within the B2 domains with negative η, while the regions with non-zero ζ appear in the B2 domains with positive η. Comparing figures 10(a-4) and 11(a), one may notice that $D0_3$-type APBs impinge the B2-type ones and triple junctions of APBs are formed at these locations. The triple junctions are observed in actual $D0_3$ domain structures formed from the initial A2 state, as shown in figures 11(b) and (c).

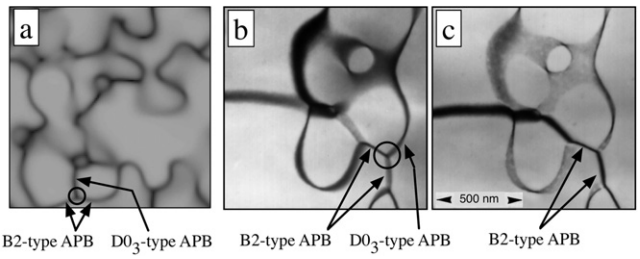

Figure 11. Two-dimensional map of $\xi^2 + \zeta^2$ in the $D0_3$ state after 35 k steps (a), and 111 (b) and 222 (c) dark field images of Fe–24.6 at.% Al alloy which was held at 743 K and then annealed at 773 K for 10 ks. Map (a) corresponds to 111 dark field images. $D0_3$-type boundaries can be distinguished from B2-type ones in image (b) with the help of (c). Note: B2- and $D0_3$-type APBs indicated by arrows meet at triple junctions in the encircled regions.

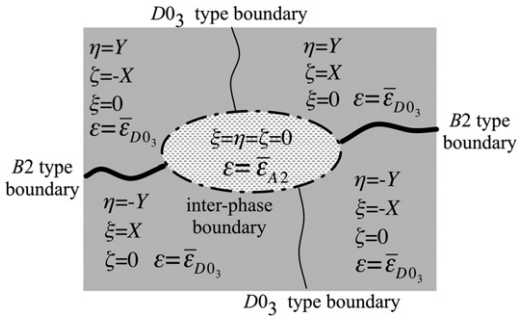

Figure 12. Parameters of order and composition within four types of $D0_3$ domains (gray portions) and an A2 phase region (a dotted portion) in the equilibrium state. Thick and thin curves indicate B2 and $D0_3$ type boundaries, respectively, while a dashed curve denotes an inter-phase boundary. The compositions $\bar{\varepsilon}_{A2}$ and $\bar{\varepsilon}_{D0_3}$ are indicated in figure 6.

When the interface tensions acting on the APBs are balanced at the triple junctions, the APBs meet at an angle θ_t given by

$$\sigma_{D0_3} = -2\sigma_{B2}\cos\theta_t, \tag{18}$$

where σ_{D0_3} is the interfacial tension of $D0_3$-type APBs and σ_{B2} is that of B2-type APBs. If the order parameters have achieved their equilibrium values (i.e. $\eta = \pm Y$ and ξ or $\zeta = \pm X$) in the domain interior, σ_{D0_3} and σ_{B2} can be evaluated as $\sigma_{D0_3} \approx \frac{1}{\Delta}\nu(2X)^2$ and $\sigma_{B2} \approx \frac{1}{\Delta}\{2\nu X^2 + \mu(2Y)^2\}$, respectively (see equation (7), figure 12, and references [5, 34]). Here Δ is the interfacial thickness. The angle θ_t is found to be $\sim$110° by using equation (18) for the simulation condition for $X \approx 0.099$ and $Y \approx 0.16$. This value is approximately equal to that of θ_t measured in the encircled region of figure 11(a). This suggests that the evaluated interfacial tensions quantitatively account for the morphology of APBs in our simulation. Since

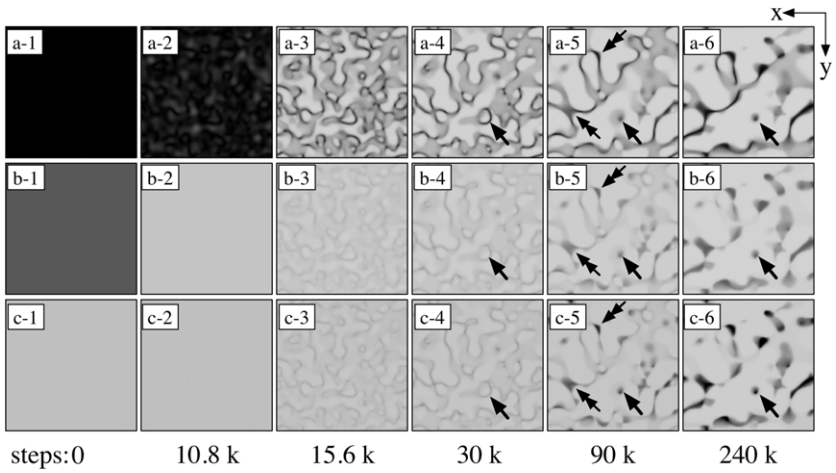

Figure 13. Concurrent ordering and phase separation from B2 to A2 + $D0_3$ at $\varepsilon = -0.025$. Spatial variations of ζ^2, η^2, and ε are two-dimensionally illustrated in the top (a), middle (b), and bottom (c) rows, respectively. Since η is initially set to be positive, $\xi \sim 0$ is considered to be held in domains according to the selection rule (see figure 4); therefore, maps of ζ^2 (a-2)–(a-6) correspond to 111 dark field images. Maps of η^2 (b) correspond to 222 dark field images. Double arrows indicate A2 precipitates formed on APBs, while single arrows show the formation of an A2 droplet due to the shrinking of an ordered domain.

$\theta_t \sim 100°$ is obtained within the encircled region in the TEM image of figure 11(b), our simulation provides a good reproduction of the domain structures in real Fe–Al alloy systems.

5.3. $B2 \rightarrow A2 + D0_3$ transition

Figure 13 shows a process of concurrent ordering and phase separation from B2 to A2 + $D0_3$. The first reaction begins with the homogeneous ordering of the B2 type and $D0_3$ domain formation, as observed in (a-2) and (b-2). No concentration variation appears at this stage. Subsequently, the $D0_3$ domains grow with the evolution of $D0_3$ ordering, as shown in (a-3) and (a-4). Simultaneously, spatial variations of η and ε also develop along with the $D0_3$ ordering. Gray lines gradually appear along the APBs between the $D0_3$ domains in the corresponding maps of (b-3), (b-4), (c-3), and (c-4). They indicate that the values of η and ε decrease along the APBs rather than within the domains. In the following stage, dark regions enriched with A atoms are found at highly curved portions of the APBs, as indicated by double arrows in (c-5). Based on figure 14(b), these dark regions are regarded to be of the A2 phase. Red iso-surfaces of ε are recognized at the corresponding regions denoted by double arrows and the values of ε are lower there than the critical composition of B2 ordering, $\varepsilon_{B2} - c_Y$. The tension of the interface boundaries between the A2 and $D0_3$ phases σ_{IPB} is balanced by σ_{D0_3} at the intersection containing the two interface boundaries and the $D0_3$-type APB;

$$\sigma_{D0_3} = 2\sigma_{IPB} \cos \frac{\theta_w}{2}, \tag{19}$$

where θ_w is the angle at which the interface boundaries intersect. If the order parameters and concentration take the equilibrium values in the domains and the A2 phase regions, σ_{IPB} can be represented by $\sigma_{IPB} \approx \frac{1}{\Delta}\{\nu X^2 + \mu Y^2 + \omega(\bar{\varepsilon}_{D0_3} - \bar{\varepsilon}_{A2})^2\}$ for the interfacial thickness Δ according to equation (7) and figure 12 [5, 34]. Here $\bar{\varepsilon}_{A2}$ and $\bar{\varepsilon}_{D0_3}$ are the compositions of phases A2 and $D0_3$, respectively (see figure 6). The angle θ_w is obtained by using the evaluated values of σ_{IPB} and σ_{D0_3} in equation (19). The approximated value ($\theta_w \sim 80°$) is reasonable for partial wetting. The A2 phase regions enlarge with time after 90 k steps and assume droplet-like shapes in figures 13(c-6) and 14(c) at 240 k steps. Some of the A2 phase droplets are in contact with the APBs of the $D0_3$ domains, while the others are isolated from the APBs. Generally, the droplets in contact with the APBs are irregular in shape, while the isolated droplets are round or oval. The formation of isolated A2 phase droplets can be observed in the figures at time steps from 30 to 240 k (figures 13(c-4)–(c-6) and 14). The domain pointed to by a single arrow is enclosed by an APB at 30 k steps, and the A2 phase is precipitated partially on the APB at 90 k steps. The domain then shrinks with time, resulting in A2 phase droplets after 240 k steps. Therefore, the A2 phase droplets are formed in the $D0_3$ domain interior in a continuous manner, which is different from the classical nucleation and growth process.

Figure 15 shows a series of TEM images showing the microstructure change during the B2 $\rightarrow$ A2 + $D0_3$ transition in Fe–24.6 at.% Al. $D0_3$-ordered domains are visible in the 111 dark field image at 0.3 ks in (a-1), while a fairly diffuse contrast appears in the corresponding 222 image in (b-1). $D0_3$-type ordering prevails throughout the specimen around this stage. From the 111 images in (a-1)–(a-4), we observe that the $D0_3$ domains grow with annealing time. The APB structure is also recognized with faint contrast in the 222 image of (b-2) at 1 ks. It suggests that the degree of B2 order takes a lower value along the APBs than that in the domain interior by the slight enrichment of Fe atoms along the APBs. The contrast of the APBs in the 222 images is enhanced after prolonged annealing for 10 ks since Fe atoms are more condensed on the APBs. It is observed in (b-4) at 100 ks that some portions of the APBs exhibit a darker contrast than other parts of the APBs. Therefore, partial wetting of the A2 phase appears to occur on the APBs due

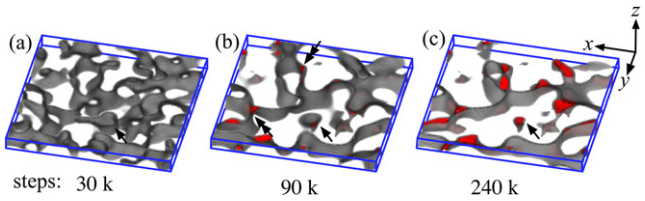

Figure 14. Three-dimensional iso-surfaces of ζ^2 (gray level) are overlapped with those of ε (red) with ten layers of grids along the z direction. The former surfaces are equivalent to $D0_3$-type APBs and correspond to figures 13((a-4)–(a-6)), while the latter ones are related to figures 13((c-4)–(c-6)). Double arrows indicate A2 precipitates formed on highly curved portions of the APBs, while single arrows show the formation of an A2 droplet due to the shrinking of an ordered domain.

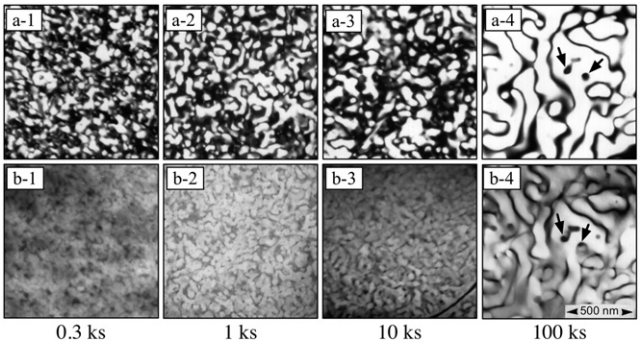

Figure 15. Microstructure change during B2 to A2 + $D0_3$ transition in Fe–24.6 at.% Al at 773 K. 111 dark field images (a) and 222 ones (b). (a-4) and (b-4) correspond to the same image field. Note: A2 phase droplets in the domain interior are indicated by arrows.

to the enrichment of Fe atoms. A2 phase droplets are found within the domains, as indicated by the arrows in (a-4) and (b-4). Since the microstructure change observed in the TEM images is well reproduced in our simulation, we can conclude that the droplets are formed in such a continuous manner by the shrinking of $D0_3$-type APBs wetted partially by the A2 phase.

5.4. A2 → A2 + $D0_3$ transition

Figure 16 presents a process of the A2 → A2 + $D0_3$ transition with phase separation. The map of η in (b-2) is mostly gray; however, that of $\xi + \zeta$ in (a-2) is completely dark. No significant modulation is recognized in the field of ε in (c-2). Therefore, the B2 ordering first develops in the entire area, independent of the concentration variations in the early stage up to 4 k steps. $D0_3$-type ordering occurs within growing B2 domains after 27 k steps. On the other hand, the maps of ε in (c-3) and (c-4) also exhibit the contours of B2 domain structures, revealing that ε takes a lower value along the B2-type APBs than in the domain interior. It is observed in (c-4) that there are some droplets with a darker contrast in parts of the B2-type APBs. These are considered to be A2 phase droplets. The contrast along the B2-type APBs in the field of ε becomes increasingly darker with an increase in

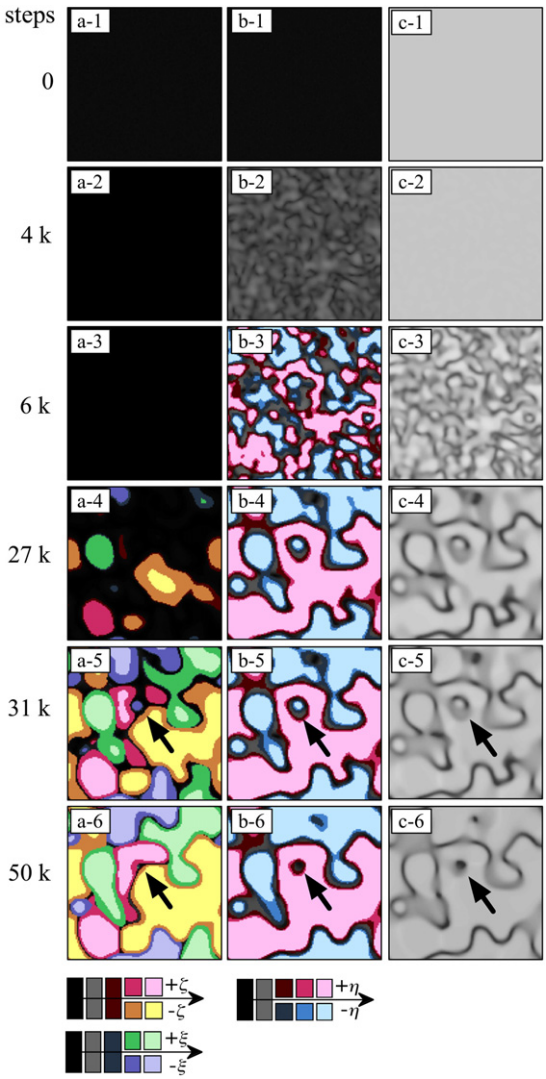

Figure 16. Time-evolution of the two-phase mixture of A2 + $D0_3$ from A2 at $\varepsilon = -0.025$. The left, center, and right columns comprise two-dimensional maps of $\xi + \zeta$ (a), η (b), and ε (c), respectively. We use different colors to distinguish four types of $D0_3$ domains in maps (a) and to indicate the sign of η in the domains in maps (b). Therefore, the wetting of the A2 phase on APBs can be easily observed. Note: the formation of A2 phase droplets is indicated by arrows.

the time step from 6 to 50 k steps. Layers of the A2 phase cover most of the B2-type APBs in (c-6). This suggests that the A2 phase perfectly wets the B2-type APBs. The perfect wetting is confirmed by the inequality $2\sigma_{\mathrm{IPB}} < \sigma_{\mathrm{B2}}$, which is derived on the condition that the order parameters and concentration have attained equilibrium values within the domains. In the maps at 31 and 50 k steps, we observe that isolated A2 droplets are formed in the domain interior due to the shrinking of closed B2 domains, as indicated by the arrows. This droplet formation process is almost the same as that observed in the previous case from B2. However, the resultant morphology in the present case is quite different from that in the previous one, since a considerable amount of the A2 phase is formed in interconnected layers wetting B2-type APBs.

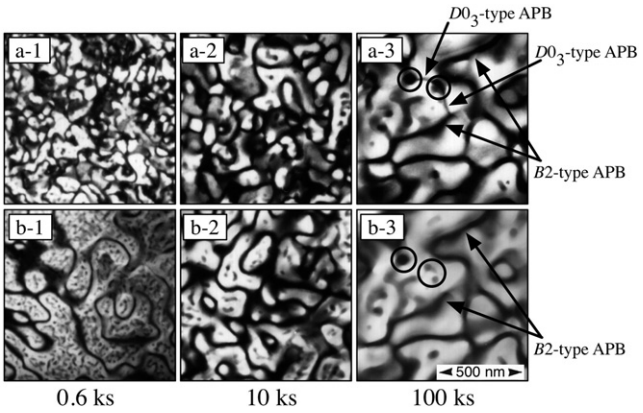

Figure 17. Microstructure change during the A2 → A2 + $D0_3$ transition in Fe–24.6 at.% Al at 803 K. 111 dark field images (a) and 222 ones (b). (a-4) and (b-4) correspond to the same image field. Note: A2 phase droplets are attached to $D0_3$-type APBs in the encircled regions.

Figure 17 shows the microstructure change in Fe–24.6 at.% Al observed in TEM images. $D0_3$ domains are recognized in the 111 image at 0.6 ks. The $D0_3$ domains coarsen as the annealing proceeds, as evident in (a-1)–(a-3). The layers with dark contrast corresponding to the B2-type APBs become thicker from (b-1) to (b-2). This suggests that the A2 phase is precipitated in the form of layers along the APBs. On the other hand, A2 phase droplets are found on $D0_3$-type APBs, as observed in (a-3) and (b-3). The domain structure is similar in appearance to that shown in (a-6) and (b-6) in figure 16. Therefore, the time-evolution of the A2 and $D0_3$ two-phase structures in an Fe–Al alloy is simulated quite well by the present kinetic model.

6. Summary

We present the TDGL formulation for the ordering processes of B2 and $D0_3$ considering the crystal symmetries of their structures. The formation of domain structures in an Fe–Al alloy system is reproduced in numerical simulations for several transition cases. For example, $D0_3$-type domains are subsequently formed within B2-type domains in the transitions A2 → $D0_3$ and A2 → A2 + $D0_3$. On the basis of the simulation results and TEM observations, we can confirm that A2 phase droplets within domains are formed in a continuous manner and B2 domains that are surrounded by the A2 phase layers in the A2 → A2 + $D0_3$ transition undergo shrinking, while the droplets result from the shrinking of $D0_3$ domains with APBs partially wetted by the A2 phase in B2 → A2 + $D0_3$.

References

[1] Oki K, Hasaka M and Eguchi T 1973 *Japan. J. Appl. Phys.* **12** 1522
[2] Marcinkowski M J and Brown N 1962 *J. Appl. Phys.* **33** 537
[3] Allen S M and Cahn J W 1975 *Acta Metall.* **23** 1017
[4] Allen S M and Cahn J W 1976 *Acta Metall.* **24** 425
[5] Allen S M and Cahn J W 1979 *Acta Metall.* **27** 1085
[6] Krzanowski J E and Allen S M 1983 *Acta Metall.* **31** 213
[7] Krzanowski J E and Allen S M 1986 *Acta Metall.* **34** 1035
[8] Krzanowski J E and Allen S M 1986 *Acta Metall.* **34** 1045
[9] Allen S M and Krzanowski J E 1986 *Solute-Defect Interaction: Theory and Experiment* ed S Saimoto *et al* (Amsterdam: Elsevier Science and Technology) p 400
[10] Park W and Allen S M 1986 *Materials Problem Solving with the Transmission Electron Microscope* (*Proc. Materials Research Society* vol 62) ed L W Hobbs *et al* (Warrendale, PA: Materials Research Society) p 303
[11] Oki K, Matsumura S and Eguchi T 1987 *Phase Transit.* **10** 257
[12] Chen L Q and Khachaturyan A G 1991 *Scr. Metall. Mater.* **25** 61
[13] Chen L Q and Khachaturyan A G 1991 *Scr. Metall. Mater.* **25** 67
[14] Chen L Q and Khachaturyan A G 1991 *Acta Metall.* **39** 2533
[15] Chen L Q, Wang Y and Khachaturyan A G 1991 *Phil. Mag. Lett.* **64** 241
[16] Chen L Q and Khachaturyan A G 1992 *Phys. Rev.* B **46** 5899
[17] Wang Y, Chen L Q and Khachaturyan A G 1992 *Phys. Rev.* B **46** 11194
[18] Chen L Q and Khachaturyan A G 1993 *Phys. Rev. Lett.* **70** 1477
[19] Dobretsov V Y, Vaks V G and Martin G 1996 *Phys. Rev.* B **54** 3227
[20] Athènes M, Bellon P, Martin G and Haider F 1996 *Acta Mater.* **44** 4739
[21] Gorentsveig V I, Fratzl P and Lebowitz J L 1997 *Phys. Rev.* B **55** 2912
[22] Le Floc'h D, Saha-Dasgupta T and Finel A 1997 *Comput. Mater. Sci.* **8** 192
[23] Belashchenko K D, Samolyuk G D and Vaks V G 1999 *J. Phys.: Condens. Matter* **11** 10567
[24] Vaks V G 2004 *Phys. Rep.* **391** 157
[25] Landau L D and Lifshitz E M 1959 *Statistical Physics* (London: Pergamon) p 430
[26] Luban M 1976 *Phase Transitions and Critical Phenomena* vol 5A, ed C Domb and M S Green (London: Academic) p 35
[27] Gunton J D, Miguel M S and Sahni P S 1983 *Phase Transitions and Critical Phenomena* vol 8, ed C Domb and M S Green (London: Academic) p 267
[28] Chen L Q 2002 *Annu. Rev. Mater. Res.* **32** 113
[29] Eguchi T, Oki K and Matsumura S 1984 *Phase Transformations in Solids* ed T Tsakalakos (Amsterdam: Elsevier) p 589
[30] Ninomiya H, Eguchi T and Kanemoto H 1990 *Phase Transit.* **28** 125
[31] Shiiyama K, Horai K and Eguchi T 1992 *Slow Dynamics in Condensed Matter* ed K Kawasaki *et al* (New York: AIP) p 537
[32] Shiiyama K, Ninomiya H and Eguchi T 1994 *Research of Pattern Formation* ed R Takaki (Tokyo: KTK Scientific Publishers) p 411
[33] Matsumura S, Tanaka Y, Müller S and Abromeit C 1996 *J. Nucl. Mater.* **239** 42
[34] Cahn J W and Hilliard J E 1958 *J. Chem. Phys.* **28** 258